Neutral Composition Information in ICON EUV Dayglow Observations

Richard Michael Tuminello[1,1], Scott L England[2], Martin M Sirk[3], Robert R. Meier[4], Andrew W. Stephan[1], Eric J Korpela[3], Thomas Immel[3], Stephen B Mende[3], and Harald U. Frey[3]

[1]U.S. Naval Research Laboratory
[2]Virginia Polytechnic Institute and State University
[3]University of California, Berkeley
[4]George Mason University

November 30, 2022

Abstract

Since the earliest space-based observations of Earth's atmosphere, ultraviolet (UV) airglow has proven a useful resource for remote sensing of the ionosphere and thermosphere. The NASA Ionospheric Connection Explorer (ICON) spacecraft, whose mission is to explore the connections between ionosphere and thermosphere utilizes UV airglow in the typical way: an extreme-UV (EUV) spectrometer uses dayglow between 54 nm and 88 nm to measure the density of O+, and a far-UV spectrograph uses the O 135.6 nm doublet and N2 Lyman-Birge-Hopfield band dayglow to measure the column ratio of O to N2 in the upper thermosphere. Two EUV emission features, O+ 61.6 nm and 83.4 nm, are used for the O+ retrieval; however, many other features are captured along the EUV instrument's spectral dimension. In this study, we examine the other dayglow features observed by ICON EUV and demonstrate that it measures a nitrogen feature around 87.8 nm which can be used to observe the neutral thermosphere.

Neutral Composition Information in ICON EUV Dayglow Observations

Richard M. Tuminello[1,2], Scott L. England[1], Martin M. Sirk[3], R. R. Meier[4,5],

Andrew W. Stephan[2], Eric J. Korpela[3], Thomas J. Immel[3], Stephen B.

Mende[3], Harald U. Frey[3]

[1]Aerospace and Ocean Engineering, Virginia Polytechnic Institute and State University, Blacksburg, VA,

USA

[2]US Naval Research Laboratory, Washington, DC, USA

[3]Space Sciences Laboratory, University of California, Berkeley, CA, USA

[4]Physics and Astronomy, George Mason University, Fairfax, VA, USA

[5]US Naval Research Laboratory (Emeritus), Washington, DC, USA

Key Points:

- A comprehensive introduction to the ICON EUV dayglow observations is presented.
- Some dim emission features are identified as originating from O^+ from similarity to known features.
- Emission near 87.8 nm follows N_2 and, combined with 61.6 nm data, allow for measurement of O/N_2.

Corresponding author: Richard Tuminello, `mtrichard@vt.edu`

Abstract

Since the earliest space-based observations of Earth's atmosphere, ultraviolet (UV) airglow has proven a useful resource for remote sensing of the ionosphere and thermosphere. The NASA Ionospheric Connection Explorer (ICON) spacecraft, whose mission is to explore the connections between ionosphere and thermosphere utilizes UV airglow in the typical way: an extreme-UV (EUV) spectrometer uses dayglow between 54 nm and 88 nm to measure the density of O^+, and a far-UV spectrograph uses the O 135.6 nm doublet and N_2 Lyman-Birge-Hopfield band dayglow to measure the column ratio of O to N_2 in the upper thermosphere. Two EUV emission features, O^+ 61.6 nm and 83.4 nm, are used for the O^+ retrieval; however, many other features are captured along the EUV instrument's spectral dimension. In this study, we examine the other dayglow features observed by ICON EUV and demonstrate that it measures a nitrogen feature around 87.8 nm which can be used to observe the neutral thermosphere.

Plain Language Summary

The ionosphere is a region of near-Earth space made up of plasma. NASA's ICON mission seeks explore the factors influencing formation of the ionosphere and how it interacts with Earth and its atmosphere. One of the ways ICON does this is by measuring airglow: light released by the air in the upper atmosphere. This occurs with visible light, with the same shades seen in the aurora; it also occurs in the ultraviolet range, invisible to the human eye but visible to ICON instruments.

An imager is included on ICON to measure extreme-ultraviolet light, almost as energetic as X-rays. Certain atoms and molecules in the atmosphere are known to glow at specific wavelengths. By measuring the brightness of airglow at certain wavelengths, ICON is able see the structure of ionospheric oxygen. The instrument also measures dimmer emissions at other wavelengths, some of which are known to come from certain atmospheric species and others which are unknown or uncertain. Here we look at the other wavelengths and attempt to find their origins. We find that most are likely coming from oxygen. Interestingly, we find one that we think comes from nitrogen. This could be useful for measuring the abundance of molecular nitrogen in the upper atmosphere, a task currently performed by another instrument on the ICON spacecraft. We make a case for the practicality of this approach.

1 Introduction

Extreme ultraviolet (EUV) dayglow has long been a phenomenon of interest in the study of the terrestrial upper atmosphere and ionosphere. Beginning with the earliest rocket measurements in the late 1960s and early 1970s (e.g. (Young et al., 1968), (Donahue & Kumer, 1971)) which include the identification of the bright 83.4 nm O^+ line produced by photoionization excitation of O (Carlson & Judge, 1973), EUV observations immediately provided a means of studying the ionosphere. Study of the terrestrial EUV dayglow continued in 1972 when the first spectral observations were taken from the lunar surface on the Apollo 16 mission (Carruthers & Page, 1976) and were followed by higher resolution spectra from rocket experiments (Christensen, 1976) (Gentieu et al., 1979). The first satellite measurements, taken from the USAF STP 78-1 spacecraft (Chakrabarti et al., 1983), combined with the rocket measurements, form the much of the basis of the modern understanding of Earth's EUV dayglow between 30 and 91 nm. EUV and far-UV (FUV) emissions longward of 91 nm have received much scrutiny, often due to the numerous atomic oxygen features found in those wavelength ranges (e.g. (Cotton et al., 1993)).

In the time intervening, some individual EUV features have seen extended study. One such example is the aforementioned 83.4 nm O^+ line, which has been observed by multiple spacecraft (notably by SSULI and RAIDS prior to ICON) and has been used to retrieve altitude profiles of ionospheric O^+ (Stephan, 2016). More recently, the 61.6 nm (sometimes referred to as 61.7 nm) O^+ feature has been proven useful for ionospheric retrieval, in part due to being optically thin in the thermosphere, where the 83.4 nm line undergoes significant scattering and absorption by O^+ in the ionosphere (Stephan et al., 2012). Additionally, the 58.4 nm He feature has been studied with some detail (e.g. (Bush & Chakrabarti, 1995), (Anderson et al., 1979)). However, outside of these few features, much of the remaining EUV spectrum has not seen much study since the initial spectroscopy experiments in the 1980s. As a result, although other lines have been observed and documented (Meier, 1991), little is known about the production mechanisms of several EUV dayglow features.

Thermospheric neutral composition has significant impact on the composition and density of the ionosphere. In particular, high O density enhances O^+ production via photoionization of O (increasing total ionospheric density) and charge exchange with N_2^+;

meanwhile high N_2 density enhances one of the primary loss processes for O^+: the reaction $O^+ + N_2 \rightarrow NO^+ + N$ (Prölss & Bird, 2004). As O^+ is the dominant ion in the F-region, the column O/N_2 ratio, $\Sigma O/N_2$ (Strickland et al., 1995), is an important quantity in the study of ionosphere-thermosphere coupling (e.g. (Lean et al., 2011) (Mendillo et al., 2005)). $\Sigma O/N_2$ is defined by (Strickland et al., 1995) as the ratio of the vertical column densities of O and N_2 above a base where the N_2 column density is 10^{-17} cm^{-2}. (Meier, 2021) discusses the column density ratio in some detail and provides the prescription for its computation. $\Sigma O/N_2$ has long been retrieved using far UV (FUV) dayglow observations of the 135.6 nm O doublet and Lyman-Birge-Hopfield (LBH) bands, starting with the AIRS instrument on the Polar BEAR spacecraft (Evans et al., 1995) through TIMED-GUVI (Meier et al., 2015), for example.

Launched in late 2019, the NASA Ionospheric Connection Explorer (ICON) seeks to further characterize Earth's low-mid latitude ionosphere and the factors that influence its formation and evolution (Immel et al., 2018). ICON hosts a suite of four instruments, three of which remotely sense atmospheric parameters using airglow in various bands. These include an EUV spectrometer, which remotely senses O^+ profiles using the known 61.6 nm and 83.4 nm lines (Stephan et al., 2017), and an FUV imager, which retrieves daytime $\Sigma O/N_2$ using the 135.6 nm oxygen and a band of LBH wavelengths (Stephan et al., 2018) (Meier, 2021).

In this work, we examine features other than 61.6 nm and 83.4 nm that are captured by the ICON EUV instrument and demonstrate that the emissions near 87.8 nm have potential utility for observing the neutral thermosphere. In Section 2.1, we delve into greater detail about the function of and data reported by the ICON EUV instrument. Section 2.2 follows with a brief description of the ICON FUV instrument with an emphasis on contrasting to the EUV instrument. In Section 3, we examine the brightness profiles of the 12 emission features reported in the Level 1 (L1) EUV data and identify the source of some of the emission features by comparing them to known lines in the dataset. In Section 4, we show that the ratio of the brightness of the 61.6 nm and 87.8 nm bins from the L1 EUV contains information about $\Sigma O/N_2$. In the concluding discussion, we state our proposed identification of the emission features in the EUV L1 data and make the case for retrieval of $\Sigma O/N_2$ from EUV observations.
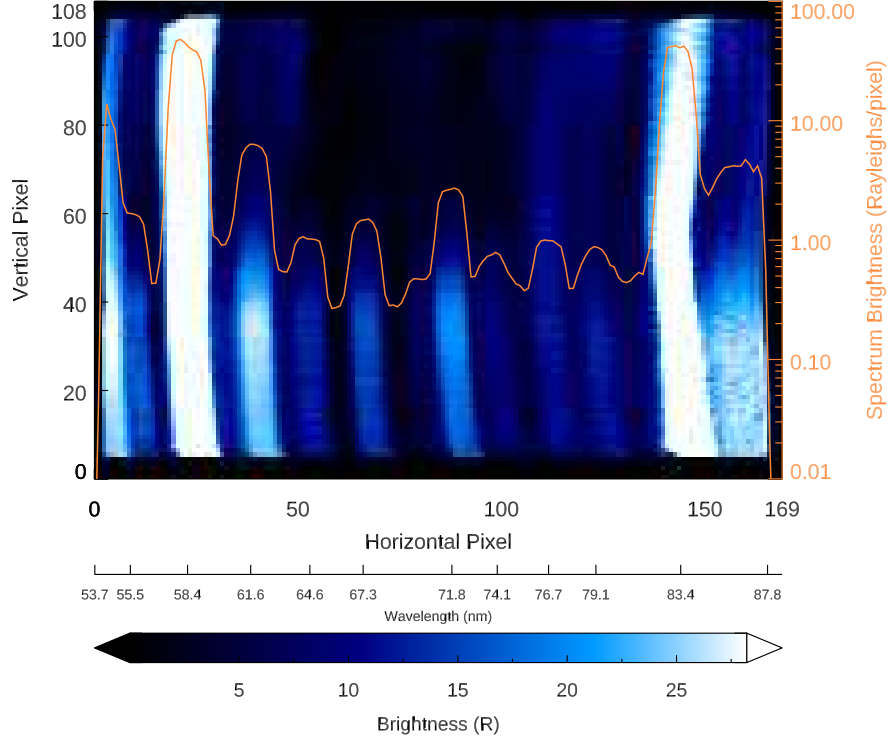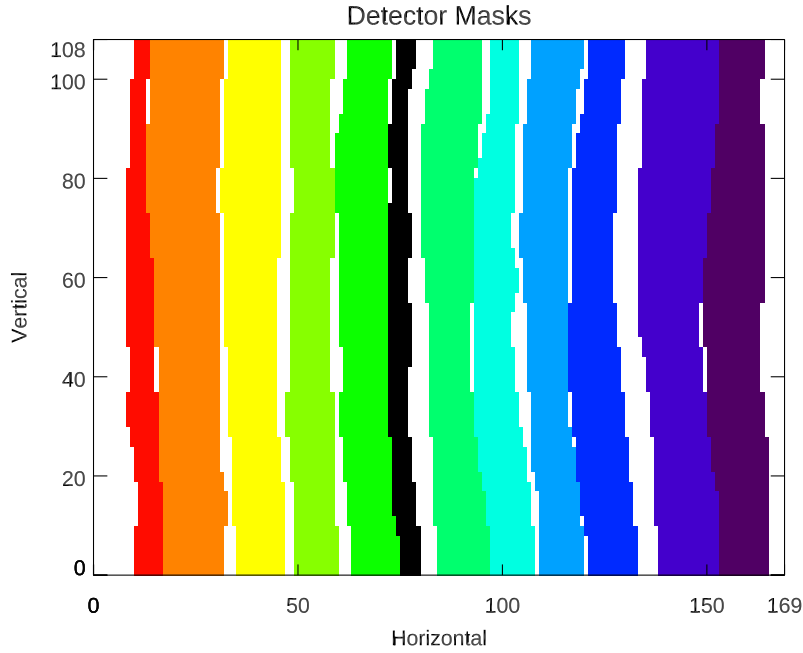
2 Data

2.1 ICON EUV

The ICON EUV instrument is a 1D imaging spectrometer, included on the ICON mission to produce O^+ density profiles in the daytime ionosphere (Sirk et al., 2017) (Stephan et al., 2017). It does so by measuring altitude profiles of O^+ airglow at 83.4 nm and 61.6 nm on the limb. During operation, EUV radiation from the atmosphere enters the instrument through a slit, illuminates a toroidal diffraction grating, and is focused onto a micro channel plate detector (MCP). The instrument was designed to have the necessary resolution to resolve the 61.6 nm O^+ line from the bright 58.4 nm He line (Sirk et al., 2017). Low level output of the instrument is a 2D array of photon counts. One dimension is 108 pixels across and spatial, oriented along the local vertical on the ICON spacecraft. The second dimension is 169 pixels across and measures wavelength. The image is flat-field corrected and the counts are converted to brightness in Rayleighs resulting in an image similar to that in Figure 1, which is the sum of all images over the course of a single day. The tall and bright features on the left and right (around 25 and 150 pixels) are the 58.4 nm and 83.4 nm lines, respectively. The 61.6 nm line is seen near pixel 45, just to the right of the 58.4 nm line.

In order to convert the brightness of each pixel to brightness of the desired emission features, masks are applied to the detector image, as depicted in Figure 2. Each mask represents a wavelength bin, intended to capture a single emission feature on the 2.1 nm resolution of the instrument. The mask boundaries were set at the minimum brightness between features, based on the first week of instrument exposure. For each row, the mask determines which pixels belong to which of the 12 wavelength bins. The variation by row, seen as distortion of emission features in pixel space (easily seen in the 83.4 nm line in Figure 1, which would otherwise be a straight vertical feature) is caused by nonuniformity in the MCP electric field. After a 12 second integration for each exposure, the pixels belonging to the same wavelength bin are summed, yielding the brightness measurement for that wavelength at a given vertical pixel. The estimated systematic error of the L1 data is 21%.

The ICON Level 1 (L1) EUV data product reports the calibrated airglow brightness along the vertical axis over the 12 second integration in 12 wavelength bins, which are tabulated in Table 1. Among these bins are three intended to capture the O^+ fea-

Figure 1. EUV detector image summed over the course of 10 June 2020. Overplotted, temporally averaged spectral brightness measured by ICON throughout 2020 for vertical pixels 35-40 (near peak brightness for most features) and 10-14 LT. The approximate wavelengths are given in Angstroms and are most accurate for the central row. Nonuniformity in the MCP electric field causes the emission features to appear curved in pixel space.

Figure 2. A visualization of the mask used to generate the L1 EUV data from the detector image. The 12 line regions are shown in color. The black region around pixel 75 is the background region, which is used to estimate the background signal.

tures at 61.6 nm and 83.4 nm and the He line centered at 58.4 nm. These lines are bright and well-known, so we will refer to them as the primary features. In higher level data products, an inversion is performed on the 61.6 nm and 83.4 nm brightness to obtain O^+ density (Stephan et al., 2017). The remaining nine bins are likewise centered around observed wavelengths and most bins contain known emissions, as indicated in Table 1. We will refer to these as secondary features. They are not part of the ICON mission objectives, but the data are there as a consequence of the resolution and passband required to measure the primary features. Nonetheless, ICON has collected a wealth of data about these features, which we examine in this study. We use the Version 03 L1 EUV Data collected over the year 2020.

In our discussion of these data, we will the tangent altitudes corresponding to each vertical pixel of the detector as the independent variable. This is a geometrical definition and does not define a unique altitude for the emitting volume elements. Indeed, the altitude of unit optical depth along the ICON line-of-sight is typically around 250 km

Table 1. Overview of the ICON EUV Bins and Known Airglow Emissions

EUV Bin Name	ICON Limb Peak Brightness (R)	ICON Disk Brightness (R)	Nominal Wavelength Range	Documented Airglow Lines	Column Emission Rate (R)
53.7 nm	51	27	54.0-55.1 nm	53.7 nm He	
				53.8 nm O^+	
				53.9 nm O^+	115
55.5 nm	9.2	3.7	55.3-56.5 nm	55.5 nm O^+	15
58.4 nm	**450**	**350**	**56.7-59.9 nm**	**58.4 nm He**	**330**
61.6 nm	**59**	**23**	**60.6-62.8 nm**	**61.6 nm O^+**	**60**
64.6 nm	9.0	3.1	63.6-65.6 nm	64.4 nm O^+	
				64.5 nm N^+	7
67.3 nm	12	4.2	66.1-68.4 nm	67.1 nm N^+	
				67.3 nm O^+	6.5
71.8 nm	23	6.8	70.6-72.5 nm	71.8 nm O^+	17
74.1 nm	6.0	2.1	72.9-74.8 nm	74.7 nm N^+	<4
76.7 nm	7.5	3.1	75.6-77.5 nm		
79.1 nm	8.4	3.4	77.7-80.0 nm		
83.4 nm	**630**	**270**	**81.2-84.1 nm**	**83.4 nm O^+**	**580**
87.8 nm	89	42	84.5-87.2 nm	87.5 nm N	<35
				88.7 nm N	<40

Primary lines are shown in **bold**. The second column contains mean peak brightness on the limb over 382,404 ICON EUV exposures between 10-14 LT from 1 January 2020 to 23 November 2020. The third contains the mean disk brightness from the monthly on-orbit flat fielding calibrations. The 53.7 nm and 87.8 nm bins are on the edge of the detector and are known to capture emissions outside of the nominal wavelength range, so relevant known emissions are included even if out of range. Additionally, the edge bins are known to suffer from vignetting of 50-75%. Nadir-viewing daytime column emission rates from 600 km are provided for previously observed lines, if available (Meier, 1991)(Chakrabarti et al., 1983). These measurements were made in 1979 near solar maximum, while the 2020 ICON measurements were made at solar minimum, so the column emission rate of the former tends to be higher.
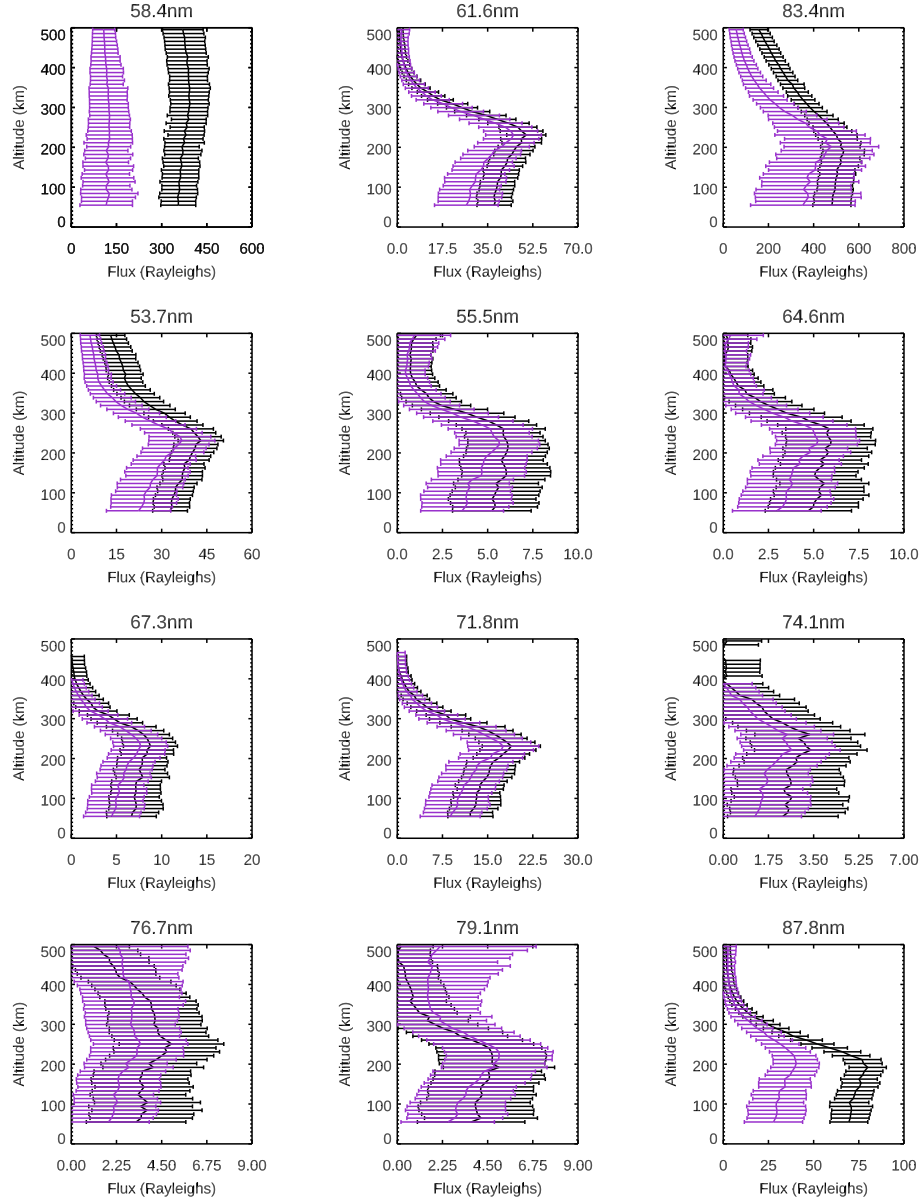
158 (due to O, O_2, and N_2 absorption, see Section 3.2), so emissions at lower tangent alti-

159 tudes come from foreground emitters above 250 km or so.

160 In order to protect the instrument from damaging particle radiation, the EUV in-

161 strument powers down when ICON passes through the South Atlantic Anomaly (SAA).

162 As a result, our dataset includes limited observations in and around the SAA. This case

163 excepted, ICON's orbit allows for full latitude-LT (local time) coverage over its 41 day

164 coverage cycle. To reduce latitude-LT coverage effects, which are expected to be dom-

165 inant over a slight seasonal bias, this analysis is restricted to 8 full coverage cycles from

166 2020 DOY 1-328.

2.2 ICON FUV

168 The ICON FUV instrument is a spectrographic imager, which observes airglow in

169 two wavelength bands (Immel et al., 2018)(Mende et al., 2017). The first passband, dubbed

170 the long wave (LW), captures a portion of the N_2 LBH emission (emitted by excited N_2

171 during the daytime) centered at 157 nm. The second, dubbed the short wave (SW), cap-

172 tures the 135.6 nm oxygen doublet, primarily emitted by excited O during the daytime

173 and by O^+ recombination at night, as well a significant (20%) contribution from another

174 portion of the N_2 LBH band. The LBH contamination in the SW channel is removed

175 in the process of retrieving the daytime Level 2 FUV product, $\Sigma O/N_2$ ratio (Stephan

176 et al., 2018).

177 While FUV observations are not the subject of this study, they are introduced as

178 means of testing the utility of EUV observations for retrieval of $\Sigma O/N_2$. We do this by

179 comparing the EUV observations to the brightness ratio SW/LW. The disk $\Sigma O/N_2$ data

180 reported in the Level 2 FUV product is not suitable for comparison because the disk pix-

181 els used for the retrieval are displaced from the EUV limb tangent points by about 15

182 degrees of latitude. However, the EUV and FUV fields of view overlap on the limb in

183 the 50-140 km tangent altitude range. We make use of this by examining the L1 FUV

184 data, which reports the SW and LW brightness profiles before the removal of the LBH

185 contribution to the SW channel and the inversion to $\Sigma O/N_2$. These measurements are

186 taken at a 12 second cadence, the same as that for the EUV instrument, although the

187 two are not synchronized. During daytime science operations, the FUV and EUV fields

188 of view are aligned horizontally.

Figure 3. Averaged altitude profiles of ICON L1 EUV wavelength bin for low (0-20, black) and high (75-90, purple) SZA, from 2020 DOY 1-328. Error bars represent the standard deviation in each altitude bin, which exceeds the Poisson error and the systematic error reported in the L1 EUV data. The top row contains the primary lines. The EUV L1 background subtraction allows for (small) negative values to be reported in the L1 product, which is why the 74.1 nm line, for example, trails off of the plot scale at high altitudes.

3 EUV Dayglow Characteristics

3.1 Altitude Profiles and Primary features

Figure 3 contains altitude-binned average profiles for each wavelength reported in the L1 EUV data for high and low solar zenith angles (SZA). We use altitude bins rather than pixel number since the tangent altitude of an individual pixel experiences some small variation due in part to the non-spherical shape of the Earth. We chose a bin size of 10 km, which is small compared to the scale height in the thermosphere (around 50 km, 30 km, and 30 km for O, O_2, and N_2, respectively) and larger than the tangent altitude spacing between pixels (2-9 km, with closer spacing at higher tangent altitudes). The former condition is important for capturing emission structure while the latter ensures that each bin is populated for each exposure. Additionally, average midday peak brightness for each emission feature on the limb and average brightness on the disk from EUV nadir-pointing calibrations are included in Table 1. First, we discuss the observations of the primary features at 58.4 nm, 61.6 nm, and 83.4 nm, since their behavior is well understood.

Emissions at 61.6 nm and 83.4 nm are each emitted by O^+ after photoionization excitation of O (Meier, 1991)(Chakrabarti et al., 1983), but their profiles differ in shape and in magnitude (83.4 nm emissions are about 10 times brighter than 61.6 nm) due to their respective production and transport mechanisms. The most significant differences are that is that 83.4 nm is produced more efficiently and undergoes multiple scattering by ionospheric O^+, while 61.6 nm is optically thin to O^+ in the ionosphere (Stephan et al., 2012).

The bright 58.4 nm line comes from resonant scattering of solar photons by neutral He (Meier, 1991). He has a very large scale height and is optically thick at 58.4 nm, so resonant scattering results in a far more uniform radiation field than if it were optically thin. The profile is essentially uniform across all ICON lines of sight and has a strong dependence on solar zenith angle, as one might expect given that solar photon scattering is a source.
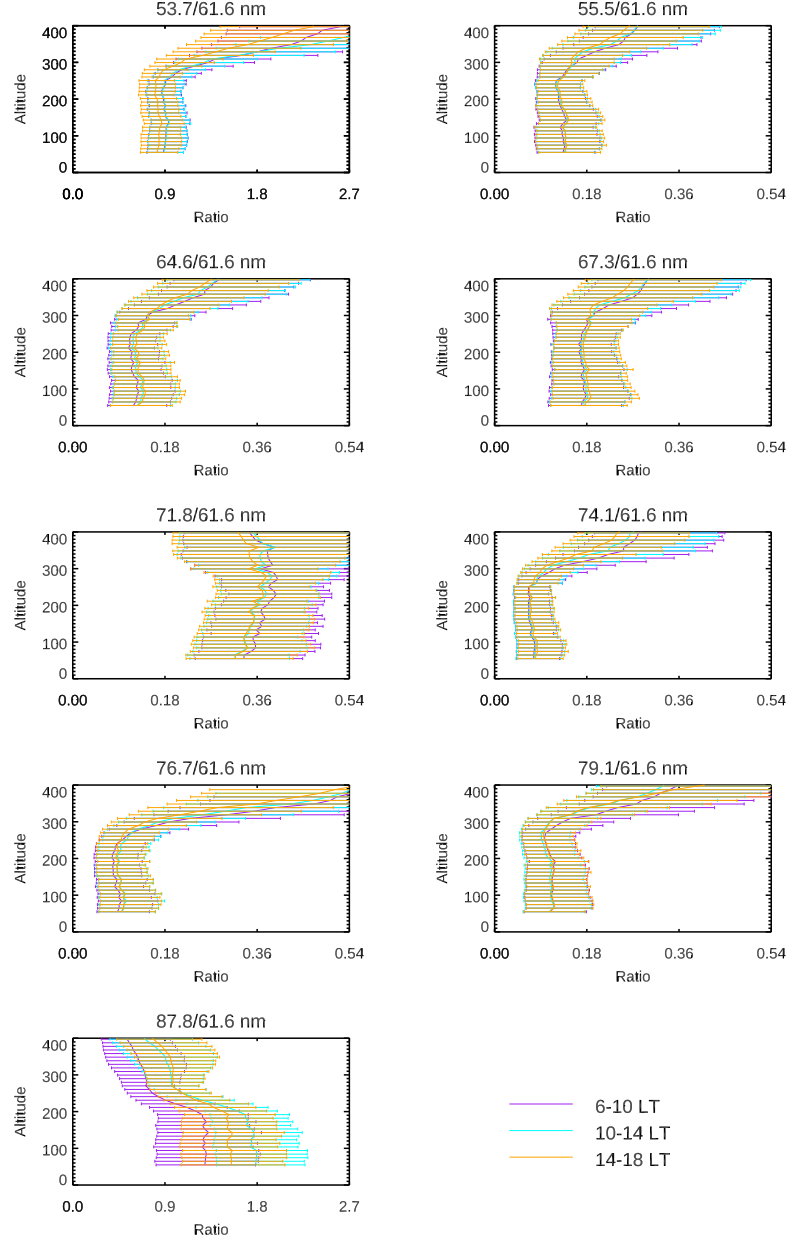
We now turn our attention to the secondary wavelengths. These emissions have been less studied, and some EUV features remain unidentified.

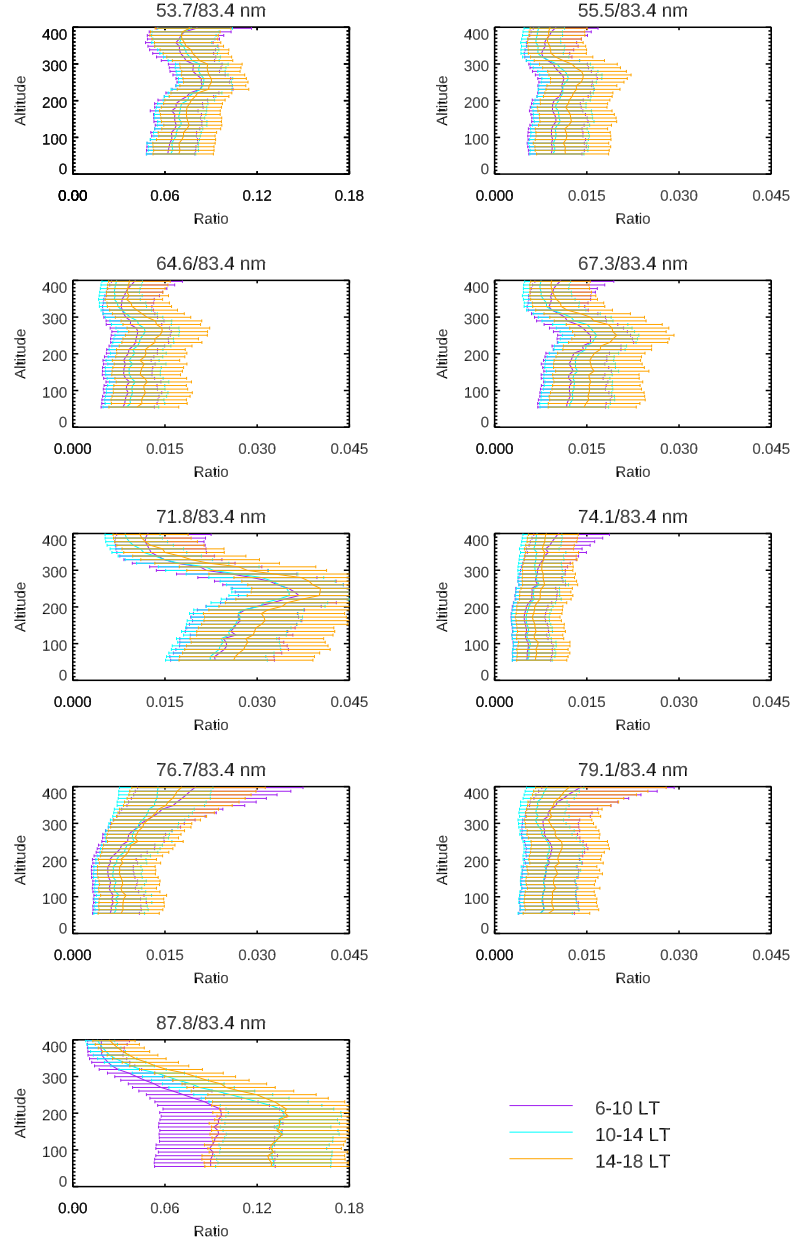### 3.2 Secondary features: Brightness Ratios and Profile Shapes

To compare one wavelength to another, it is useful to look at the brightness ratio at the time of measurement as a function of altitude. By using the ratio of individual measurements rather than the ratio of the average brightness, the variation due to differing production processes can be isolated from variation due to other factors, such as solar flux, local time, solar zenith angle, and physical location. In a further effort to isolate the sources of variation, we break down the ratios by local time and solar zenith angle. Measurements (on a single vertical pixel basis) are excluded if the brightness of the primary feature is below 5 Rayleighs or if the brightness of the secondary feature does not exceed 1 Rayleigh. We use the same scheme for altitude bins that we used for the altitude profiles. Since the brightness ratio measurements are not normally distributed and are heavily right skewed, we take the median value in each bin and represent the error as the 15.866 and 84.134 percentiles, which are equivalent to the $\pm 1\sigma$ range for normally distributed data.

The brightness ratios relative to the 61.6 nm and 83.4 nm lines and broken down by local time are shown in Figures 4 and 5. The remaining ratio plots, broken down by solar zenith angle and month and including the ratio to 58.4 brightness are contained in Appendix A. The most immediately noticeable trend in Figure 4 is that these ratios increase significantly at high altitude for most wavelengths. This is surprising because we would expect the brightness of features other than 58.4 nm and 83.4 nm to be essentially zero at and above around 400 km. The increase of the ratio of all of these features to 61.6 nm is likely the result of an small error in the absolute calibration of the instrument or in the background subtraction, which could result in a bias that would disproportionately affect the dimmer features. Since we are dividing by the small 61.6 nm brightness at high altitudes, an unnoticeable error in the flux could create a large error in the ratio. Another explanation would be that these features all scatter more efficiently than 61.6 nm or have a H or He source. It is unlikely that this holds for all features, as we will see that most of these are O features.
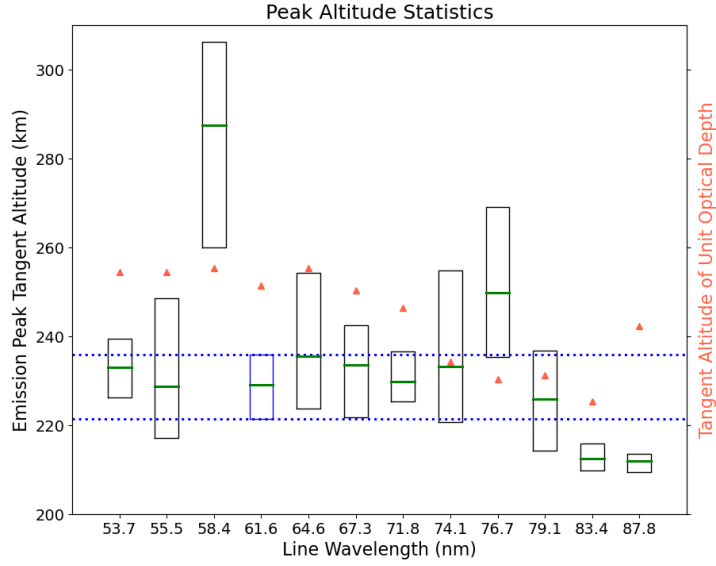
A vertical line in which the ratio is constant with little coherent variation between local times means that the brightness ratio of the primary and secondary feature is fixed and suggests that the emissions have the same or a similar source. Most of the secondary features resemble 61.6 nm in this way at low altitudes, suggesting that O could be their

Figure 4. Brightness relative to 61.6 nm brightness for each secondary line, broken down by LT. Many of these features track well with 61.6 nm at low altitude but diverge at higher altitudes.

Figure 5. Brightness relative to 83.4 nm brightness for each secondary line, broken down by LT.
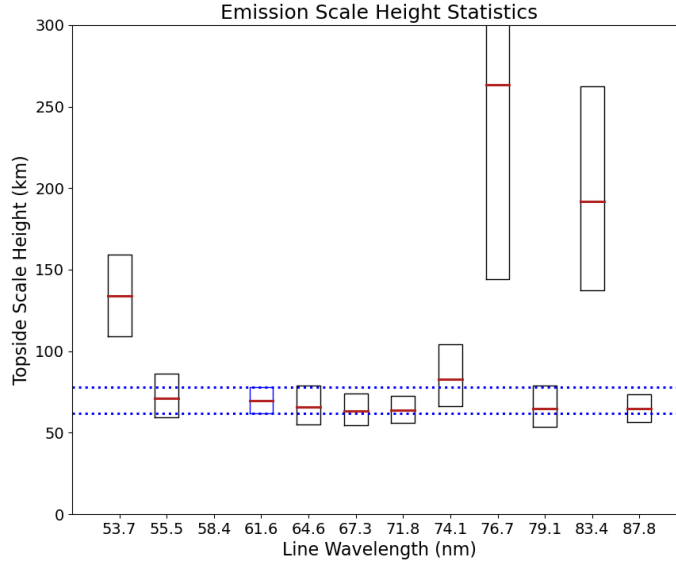
Figure 6. Green lines represent the median altitude of the emission peak for each L1 line. The upper and lower quartiles are indicated by boxes for all emissions and by the dotted blue line for the 61.6 nm line. Red triangles indicate the tangent altitude at which the tangent point reaches unit optical depth from neutral absorption along the ICON line of sight.

source. However, the altitude profile of the emission is also affected by atmospheric absorption and the scattering properties of each feature.

Approaching the peak from above, brightness increases as the line of sight begins to pass through regions with higher density of the emission source. As the line of sight pierces lower altitudes, three factors begin to determine the shape of the profile. First, the increase in overall density leads to increases in absorption/scattering between the source and the satellite. Second, production ceases to increase at the same rate as the density as the solar EUV flux is attenuated. Third, lines of sight with tangent altitudes below the production peak will see decreased brightness as the slant path through the production layer shortens. If two features have the same source, the first factor will shape the profiles differently, as scattering and absorption cross sections are wavelength dependent; and the second can also have a differing effect, solar flux is attenuated unevenly across all wavelengths, and photoionization cross sections are likewise wavelength dependent.

Figure 7. Red lines represent the median topside emission scale height (see Section 3.2) for each L1 line. The upper and lower quartiles are indicated by boxes for all emissions and by the dotted blue line for the 61.6 nm line. Given the nature of the line and the large He scale height, the lower quartile, median, and upper quartile of the 58.4 nm topside emission scale height far exceed the plot range with values of 700, 1600, and 4000 km, respectively. The upper quartile of the 76.7 nm scale height has exceeded the plot range with a value of 480 km.

Figure 6 shows the statistical location of the peak of each L1 feature, as determined by a three altitude pixel rolling average. The altitude of the peak indicates where the three factors discussed above begin to dominate over the increasing density along the line of sight. We focus on comparison to 61.6 nm since Figure 4 show that many features have similar altitude structure. We use an MSIS atmosphere and lab-measured neutral absorption cross sections (Conway, 1988) to determine the optical depth of the tangent point, and Figure 6 shows the tangent altitude at which the slant path between the tangent point and ICON has unit optical depth from absorption by O, O_2, and N_2. This allows for a simple comparison of the expected neutral absorption affects between wavelength bins; although it should be noted that the cross sections used are of low resolution (0.1-0.3 nm), and small scale structure is known to exist in parts of the EUV instrument's spectral range (see (Fennelly & Torr, 1992), for example).

We are also interested in the shape of the emission profile above the peak, where we expect the brightness to correspond most strongly to production and, thus, number density of the parent species. To parameterize the shape, we treat the brightness similarly to a density, fitting to an exponential $I = I_0 e^{\Delta z/H} + b$ to find the scale height H, allowing for some bias b to account for bias in the background subtraction. We fit only between the peak and 350 km, as the signal to noise ratio is very low above this altitude. Figure 7 contains the scale height statistics.

Looking at Figures 4 5, 6, and 7, together, we can comprehensively relate the behavior of the secondary features to that of the primary features. In Figure 4, we see that the only feature which clearly behaves differently from 61.6 nm is the 87.8 nm feature which undergoes a large shift around the 61.6 nm peak. In Figure 6, we see that the 53.7, 55.5, 67.3, and 71.8 features have a peak in family with 61.6 nm while undergoing similar absorption. Figure 7 shows that the scale height of these emissions is also in family with 61.6 nm, except for 53.7 nm, which is significantly higher. This confirms that the 55.5, 67.3, and 71.8 nm L1 bins are dominated by the known O^+ emissions (see Table 1) and that 53.7 nm is mostly O^+ with He contamination at high altitudes.

The 64.6 nm feature peaks noticeably higher than 61.6 nm while undergoing similar absorption. The scale height is similar to that of 61.6 nm, so it is likely that ICON is mostly seeing the O^+ line at 64.4 nm. However, contamination by the nearby known N^+ emission would not explain the raised peak, as we would expect N_2 rather than atomic nitrogen to be the effective source of such an emission. This also applies to the 74.1 nm feature (containing a known N^+ emission) , which peaks slightly above 61.6 nm while being optically thin to a lower altitude and has a larger scale height than 61.6 nm.

The 79.1 nm feature peaks slightly lower than 61.6 nm, but is also optically thin to a lower altitude (see Figure 6), which would have the effect of lowering the peak. Given the constant ratio to 61.6 nm at low altitudes and that the scale height is similar to that of the O^+ features, this could be a previously unidentified O or O^+ feature.

In Figure 5, the suspected O/O^+ features (53.7, 55.5, 67.3, 71.8, and 79.1 nm) all have a bump around 250 km tangent altitude that is most pronounced in the afternoon. The multiple scattering of 83.4 nm photons by O^+ has the effect of broadening the altitude profile. For this reason, the 83.4 nm profile is smoother in the afternoon than in the morning (see Figure A1) when the O^+ concentration is higher. The aforementioned

309 wavelengths are optically thin to O^+, resulting in a sharper peak and an enhancement

310 relative to 83.4 nm near the peak.

311 The 76.7 nm feature is a clear outlier. It peaks well above 61.6 nm, despite hav-

312 ing a lower tangent altitude of unit optical depth. As seen in Figure 7, the scale height

313 of this emission is very large. Figure 3 indicates that this feature has a strong SZA de-

314 pendence. While this feature is very dim, it is brighter than the 74.1 nm feature, which

315 has a well-defined shape, so this is probably a real signal. The source of this signal is un-

316 clear.

317 Another outlier is the 87.8 nm feature. This (relatively) bright feature (see Figure

318 3) peaks lower than any other at around 210 km, while undergoing similar absorption

319 to 61.6 nm (see Figure 6). This is most similar to the 83.4 nm line, but Figure 7 indi-

320 cates that 87.8 nm has a much smaller scale height than 83.4 nm and a slightly smaller

321 one than 61.6 nm. These indicators are consistent with an emission coming from a heav-

322 ier species, like N_2. In fact, N features have previously been observed at at 87.5 nm and

323 88.7 nm (Chakrabarti et al., 1983); it is likely that these are produced by excited N^* or

324 N^{+*} from photodissociation N_2, as has been observed in nearby emission features (Meier

325 et al., 1991) . In Section 4, we will show that that this bin is picking up nitrogen emis-

326 sions by establishing that the brightness ratio of 61.6 nm and 87.8 nm emissions acts as

327 a proxy for $\Sigma O/N_2$.

4 Relationship of 61.6/87.8 to $\Sigma O/N_2$

329 A common metric for tracking upper-atmospheric composition is $\Sigma O/N_2$ ratio, ob-

330 tained by a column integral of number density (n) down until a threshold N_2 column den-

331 sity ($\mathbf{N}$) of $10^{17}\,\mathrm{cm}^{-2}$ of reached, at altitude z_{17}.

$$\Sigma O/N_2 = \frac{\int_{z_{17}}^{\infty} n_O \, dz}{\int_{z_{17}}^{\infty} n_{N_2} \, dz} = \frac{\int_0^{\mathbf{N}_O} d\mathbf{N}'_O}{\int_0^{\mathbf{N}_{N_2}} d\mathbf{N}'_{N_2}} = \frac{\mathbf{N}_O}{10^{17}\,\mathrm{cm}^{-2}} \tag{1}$$

332 The altitude z_{17} is typically the 130-140 km range but is not considered to be of inher-

333 ent physical significance (Meier, 2021).

334 As stated in Section 2.2, one of the motivations for the inclusion of the FUV in-

335 strument on the ICON mission is to measure $\Sigma O/N_2$ using airglow emissions of O at 135.6

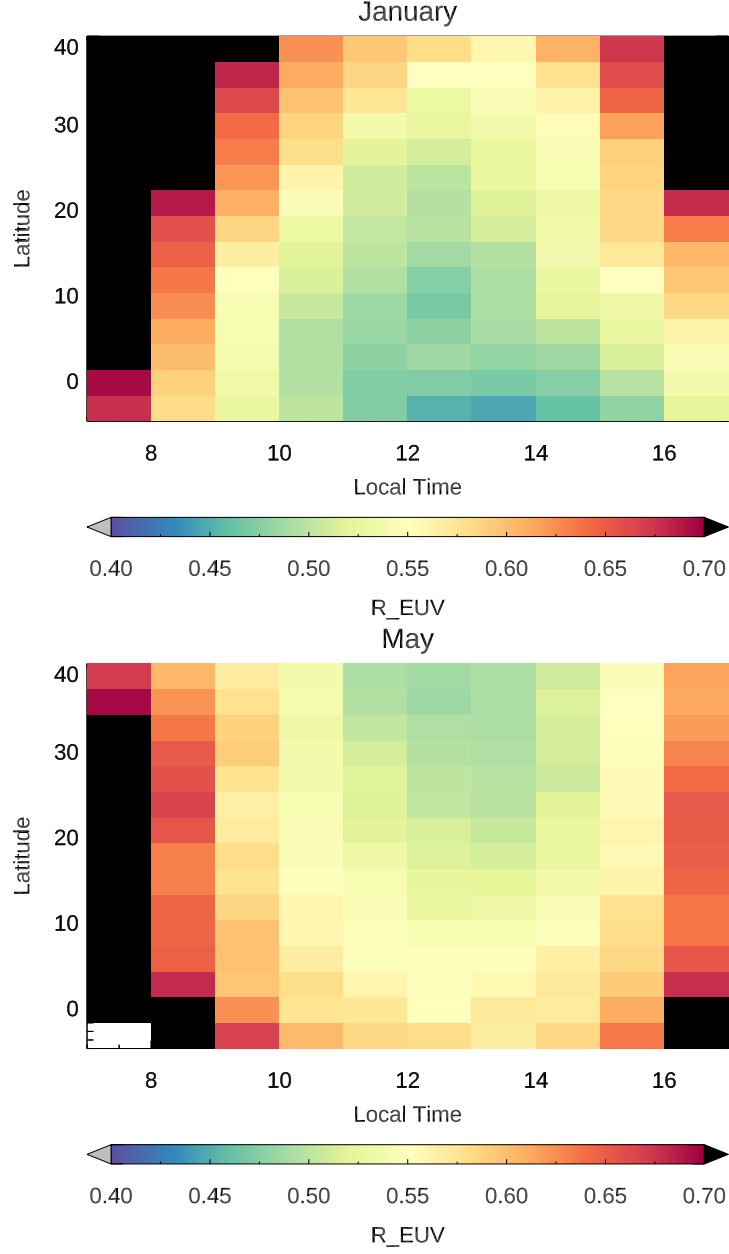336 nm (short wave, SW) and the N_2 LBH band near 157 nm (long wave, LW). The inver-

337 sion process is complex, depending on external factors such as solar zenith angle, solar

338 flux, and viewing angle. However, for a given set of observation conditions, $\Sigma O/N_2$ on

339 the disk is established to be determinable by the brightness ratio I_{SW}/I_{LW} (Meier, 2021)

340 (Strickland et al., 1995).

341 Because O is the parent source of the 61.6 nm emission and the 87.8 nm feature

342 is likely from one or both known N lines with an N_2 parent, we expect the brightness

343 ratio of the 61.6 nm and 87.8 nm bins to likewise provide a measurement of $\Sigma O/N_2$. If

344 the instrument observes low enough tangent altitudes, below the point of extinction, our

345 observation will share a key property with disk observations: the line of sight will pass

346 through all relevant altitudes once without contributions from beyond the foreground

347 (that is, beyond the tangent point).

348 The FUV features are far brighter than either of these EUV emissions. As seen in

349 Table 1, midday 61.6 nm emissions typically peak around 60 Rayleighs and 87.8 emis-

350 sions around 90 Rayleighs. In contrast, the FUV SW and LW measurements typically

351 peak around 8000 and 2000 Rayleighs, respectively. Any attempt to retrieve $\Sigma O/N_2$ us-

352 ing a single vertical pixel on the EUV detector will be dominated by shot noise. There-

353 fore, we must not only look low enough to have a disk-like measurement but also sum

354 over a range of vertical pixels so that we have sufficient signal. To do this, we define a

355 sub-limb region, which contains lines of sight with tangent point altitudes between 50

356 and 140 km. The lower boundary is approximately the lower limit of the EUV field of

357 view. With ICON's viewing geometry, we expect the tangent points to have unit opti-

358 cal depth from neutral absorption at a tangent altitude of around 240 km for both of these

359 wavelengths, so the upper boundary of 140 km tangent altitude is well within the region

360 where emissions beyond the tangent point do no significantly contribute to the measure-

361 ment (as in a disk measurement). In analogy with SW/LW, we define a simple metric

362 to compare to $\Sigma O/N_2$:

$$R_{EUV} = \frac{\sum_i I_{616,i}}{\sum_i I_{878,i}} \text{ for } i \text{ such that } z_i \in [50, 140] \, \text{km} \tag{2}$$

363 Here $I_{616,i}$ and $I_{878,i}$ are the 61.6 nm and 87.8 nm brightnesses and z_i the tangent al-

364 titude of the ith pixel of the EUV detector. We will show that R_{EUV} show is correlated

365 to $\Sigma O/N_2$, supporting our claim that the 87.8 nm feature comes from one or more N

366 emissions and suggesting the possibility of observing $\Sigma O/N_2$ using EUV observations.

Figure 8. A comparison of the latitude-LT structure of R_{EUV} for January and May 2020. The color of each pixel represents the median R_{EUV} value in the month, LT, and latitude indicated, and white pixels indicate missing data. The figures show a reversal of the latitude structure around local noon, qualitatively similar to what we would expect from $\Sigma O/N_2$.

4.1 Latitude Structure of R_{EUV} and Comparison to MSIS $\Sigma O/N_2$

One of the key characteristics of N_2 in the upper atmosphere is the seasonal variation of its spatial structure. In the summer hemisphere, increased temperature leads
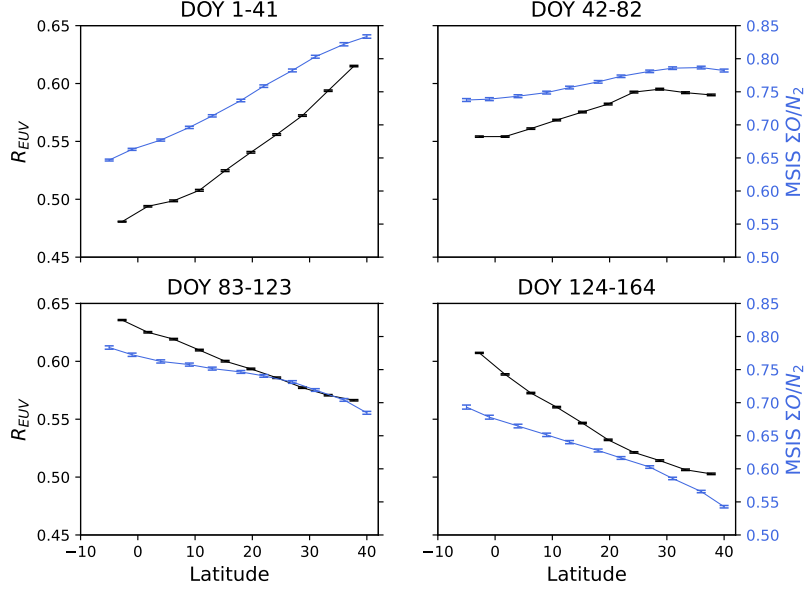
370 to a larger scale height, resulting in enhanced density of heavier species at high altitude.

371 Figure 8 shows the latitude-LT structure of R_{EUV} in January and May 2020. Both plots

372 show an increased ratio near sunrise and sunset. However, the latitudinal pattern dif-

373 fers between the two. In January, R_{EUV} is lowest around the equator and increases with

374 latitude. In May, the trend is reversed, with low R_{EUV} at mid-latitudes and higher ones

375 near the equator. We would expect to see the same qualitative trends from $\Sigma O/N_2$, and

376 such behavior has indeed been observed in $\Sigma O/N_2$ retrieved from FUV observations (Strickland

377 et al., 2004).

378 To provide a more convincing resemblance to $\Sigma O/N_2$, we now compare R_{EUV} to

379 NRLMSISE-00 (MSIS) (Picone et al., 2002) $\Sigma O/N_2$ for some consecutive 41 day cov-

380 erage cycles of ICON. Since we are mostly interested in the evolution of the latitudinal

381 structure, we reduce the EUV data to one dimension by averaging into latitude bins over

382 10-14 LT. We run MSIS at five UTCs each day at 11 equally spaced latitudes from -5

383 to 40 degrees, to match the latitudes covered by ICON. At each UTC and latitude, we

384 run MSIS for longitudes corresponding to 10, 12, and 14 LT. We use a constant F10.7

385 of 70 sfu, since the variation in F10.7 during the first half of 2020 was very small (rang-

386 ing from 68-75 sfu over the dates considered). Finally, we use a constant magnetic in-

387 dex (A_p) of 4 as this adequately characterizes the solar-quiet conditions from the first

388 half of 2020. $\Sigma O/N_2$ is averaged at each latitude, resulting, in combination with the ICON

389 data, in the plots in Figure 9.

390 There is a clear resemblance between the EUV and MSIS data in the evolution of

391 structure from winter to summer. We conclude that R_{EUV} does vary with $\Sigma O/N_2$ on

392 seasonal timescales.

4.2 Comparison of R_{EUV} to ICON FUV Data

394 The ICON FUV data provides simultaneous measurements to compare to R_{EUV}.

395 However, due to differences in viewing geometry, the location of the EUV sub-limb and

396 the disk $\Sigma O/N_2$ observations are too far apart, separated by about 14 degrees of lati-

397 tude. Fortunately, the EUV and FUV detectors overlap in the 50-140 km tangent alti-

398 tude range so we can investigate the correlation between the two. We define R_{FUV} as
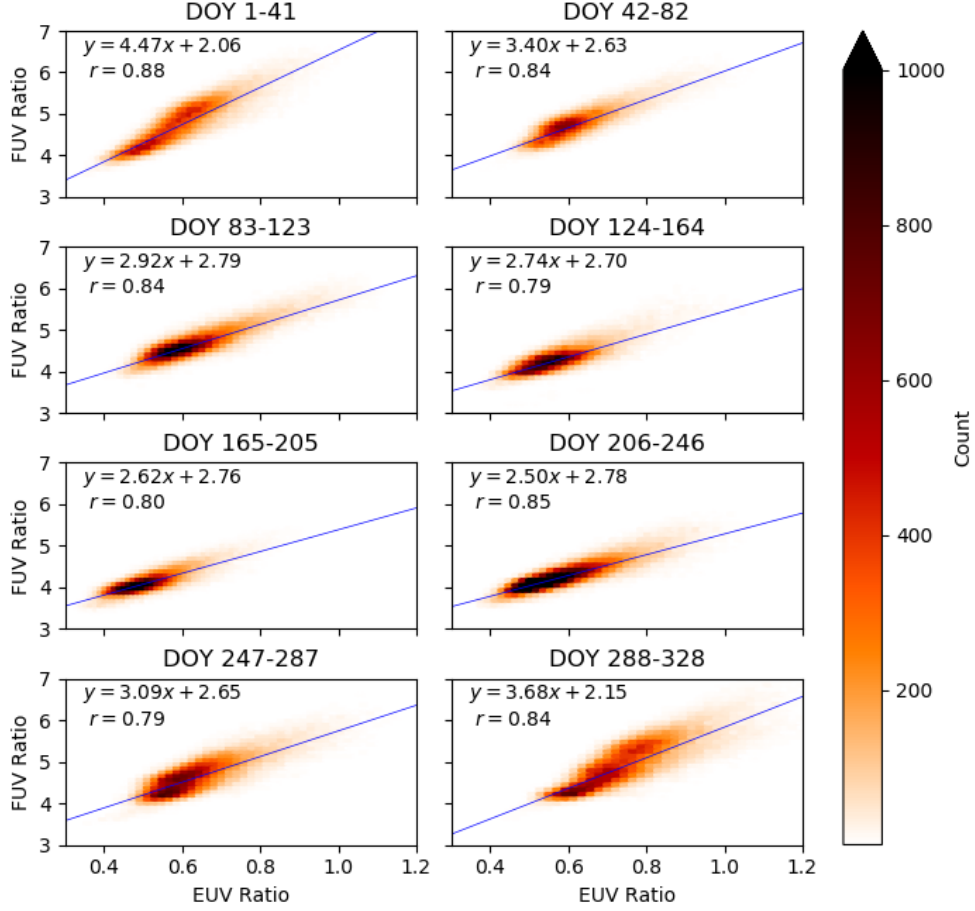
399 the ratio of mean SW and LW brightness:

Figure 9. R_{EUV} is plotted along with MSIS column O/N_2 versus latitude for 10-14 LT and date ranges from January to June. Error bars represent uncertainty in the mean. R_{EUV} is shown to undergo the same seasonal reversal seen in $\Sigma O/N_2$.

$$R_{FUV} = \frac{\sum_i I_{SW,i}/N_{SW}}{\sum_j I_{LW,j}/N_{LW}} \left\{ \begin{array}{l} \text{for } i \text{ such that } H_{SW,i} \in [50, 140]\,\text{km} \\[2ex] \text{for } j \text{ such that } H_{LW,j} \in [50, 140]\,\text{km} \end{array} \right. \quad (3)$$

Here, $H_{SW,i}$ and $H_{LW,i}$ are the tangent altitudes of the i$^{\text{th}}$ pixel in the SW and LW channels, respectively, which differ slightly due to the FUV instrument optics. N_{SW} and N_{LW} are the number of pixels that fall within the desired altitude range in the SW and LW channels. We are taking the ratio of the mean brightness here, since N_{SW} and N_{LW} can differ.

Since the fields of view are aligned between the two instruments (nominally and upon inspection), we need only look for coincidences in time. For each EUV exposure, we find the time of the nearest FUV exposure and consider the measurements coincident if the time difference is less than 12 seconds, which is the cadence of both detectors. The coincident measurements for ICON coverage cycles from 2020 DOY 1-328 are plotted in Figure 10.

Figure 10. Density plots of correlation between R_{EUV} and R_{FUV} during the eight full coverage cycles of 2020. The range in R_{EUV} varies between cycles: for example DOY 124-164 in the spring covers a small range, while DOY 1-41 in the winter covers a larger range.

⁴¹¹   Each EUV and FUV measurement has a reported uncertainty, which propagates

⁴¹² to R_{EUV} and R_{FUV}. When measuring the correlation between the datasets, we would

⁴¹³ like to give greater consideration to measurements with lesser uncertainty. Since there

⁴¹⁴ is uncertainty in the x and y variables, a typical chi-squared minimization will not do.

⁴¹⁵ Instead, we compute a fit to each curve using orthogonal distance regression (Boggs &

⁴¹⁶ Donaldson, 1989), which minimizes the orthogonal distance to the fit line and weights

⁴¹⁷ the points as the inverse square of the uncertainty. We then use these same weights to

⁴¹⁸ calculate the weighted Pearson correlation coefficient. The resulting fit is shown for the

Table 2. Weighted Pearson correlation coefficients for R_{EUV} and R_{FUV}

	6-8 LT	8-10 LT	10-12 LT	12-14 LT	14-16 LT	16-18 LT	6-18 LT
DOY 1-41	0.75	0.92	0.92	0.90	0.87	0.73	0.88
DOY 42-82	0.73	0.78	0.64	0.66	0.74	0.74	0.84
DOY 83-123	0.71	0.75	0.62	0.60	0.66	0.70	0.84
DOY 124-164	0.81	0.78	0.67	0.62	0.72	0.76	0.79
DOY 165-205	0.88	0.85	0.76	0.72	0.74	0.76	0.80
DOY 206-246	0.80	0.78	0.66	0.70	0.80	0.83	0.85
DOY 247-287	0.71	0.80	0.72	0.63	0.71	0.61	0.79
DOY 288-328	0.78	0.89	0.88	0.82	0.84	0.77	0.84
DOY 1-328	0.87	0.86	0.81	0.79	0.81	0.80	0.83

The color of each cell scales with the value, included for easy comparison with Table 3.

Table 3. 5th-95th percentile range of R_{EUV}

	6-8 LT	8-10 LT	10-12 LT	12-14 LT	14-16 LT	16-18 LT	6-18 LT
DOY 1-41	0.27	0.41	0.30	0.25	0.25	0.23	0.35
DOY 42-82	0.30	0.25	0.16	0.14	0.19	0.22	0.34
DOY 83-123	0.35	0.26	0.19	0.17	0.18	0.25	0.37
DOY 124-164	0.40	0.32	0.21	0.18	0.20	0.24	0.31
DOY 165-205	0.36	0.26	0.17	0.16	0.21	0.25	0.27
DOY 206-246	0.36	0.25	0.18	0.17	0.22	0.30	0.35
DOY 247-287	0.37	0.32	0.21	0.17	0.20	0.23	0.36
DOY 288-328	0.38	0.47	0.35	0.27	0.30	0.30	0.41
DOY 1-328	0.49	0.41	0.32	0.29	0.31	0.32	0.41

Here, the color of each cell scales with the value but clips at 0.4, so that lower values can more easily be distinguished. We can see that regions of Table 2 with low correlation coefficients generally correspond to regions of low R_{EUV} spread in Table 3.

data in Figure 10, and the correlation coefficients are tabulated in Table 2, broken down by ICON coverage cycle and local time.

The correlation between R_{EUV} and R_{FUV} is generally quite strong. The full dataset shows a correlation coefficient of 0.83. Smaller subsets restricted to a two hour local time range for a given coverage cycle show correlation coefficients as high as 0.92 and no lower than 0.60. Possible origins of variance between R_{EUV} and R_{FUV} include ionospheric contamination of the SW (135.6 nm photons produced by radiative recombination), differing atmospheric extinction between the correspondent EUV and FUV features, and noise in the EUV measurements.

There is a pattern in the correlation strength where the correlation coefficients are lowest around local noon and near equinox. The second and third panels of Figure 9, indicate that there is little variation in R_{EUV} with latitude during the spring, one of the periods with low correlation coefficients. Table 3 captures the spread of R_{EUV} within each subset of the data, and the color of each cell scales with the value. Tables 2 and

3 match up quite well, indicating that the correlation between R_{EUV} and R_{FUV} is weaker when only a small range of R_{EUV} values are considered. The exception is a dawn, when we would expect the EUV measurements very dim and, therefore, noisy.

5 Summary and Discussion

5.1 Identity of Emission Features

In Section 3.2 we showed that several emission features in the ICON EUV data behave similarly to 61.6 nm O^+. Specifically, the 53.7, 55.5, 67.3, and 71.8 nm bins are dominated by optically thin O^+ airglow.

The 53.7 nm bin is likely picking up one of the previously identified lines at 53.8 nm and/or 53.9 nm. However, its dimness relative to the 61.6 brightness calls into question the previously published column emission rate of 115 Rayleighs (Chakrabarti et al., 1983) for the 53.9 nm line. Similarly, the 55.5 nm and 71.8 nm features observed by ICON are likely the known O^+ lines at the same wavelengths. In the former case, ICON data are once again reporting a dimmer feature than anticipated. However, in the the latter case, the disk brightness from the ICON nadir calibrations is lower than the previously reported value, while the peak on the limb is about 30% brighter, a quirk that is shared with the He 58.4 nm emission. The previous measurements were made during a period of much higher solar activity, so further qualitative analysis is required to judge the compatibility of these ICON measurements with previous work.

The 67.3 nm bin is likely picking up the known O^+ emission at the same wavelength and a negligible amount of the N^+ line at 67.1 nm.

Our analysis in Section 4 has linked the 87.8 nm bin to N_2. It is likely that the bin is dominated by some combination of the known N multiplets between 86.5 nm and 88.9 nm or even the N^+ doublet near 86.0 nm (Kramida et al., 2021). These emissions are not well modeled, but the connection to N_2 suggests that one or both of these features are produced in the thermosphere by photodissociation of N_2 resulting in excited N^* (or N^{+*}), as has been observed in the lab and in the dayglow (Meier et al., 1991). As with other N and N^+ EUV emissions, photoelectron impact excitation may also contribute to the excitation rate.

It must be noted that this region on the edge of the detector is subject to an unknown amount of vignetting, which makes it difficult to interpret the absolute magnitude of the ICON measurements. Additionally, there is concern that this region of the detector may suffer from Ly-α scattering within the instrument, which would affect the shape of the profile since it would disproportionately brighten pixels at higher tangent altitudes.

5.2 Utility of R_{EUV} for Retrieving $\Sigma O/N_2$

The correlation of R_{EUV} with R_{FUV} indicates that the EUV and FUV sub-limb observations contain the same information about $\Sigma O/N_2$. In principle, this is sufficient to conclude that the EUV instrument is capable of $\Sigma O/N_2$ retrieval, since FUV sub-limb observations are known to be sufficient for inversion to $\Sigma O/N_2$ (Meier, 2021). However, the lack of an EUV dayglow model for the observed 87.8 nm feature presents an obstacle to the development of an inversion algorithm. It is likely that the ICON EUV limb observations could also provide measurements of neutral density altitude profiles, as has been done using FUV observations (Meier et al., 2015).
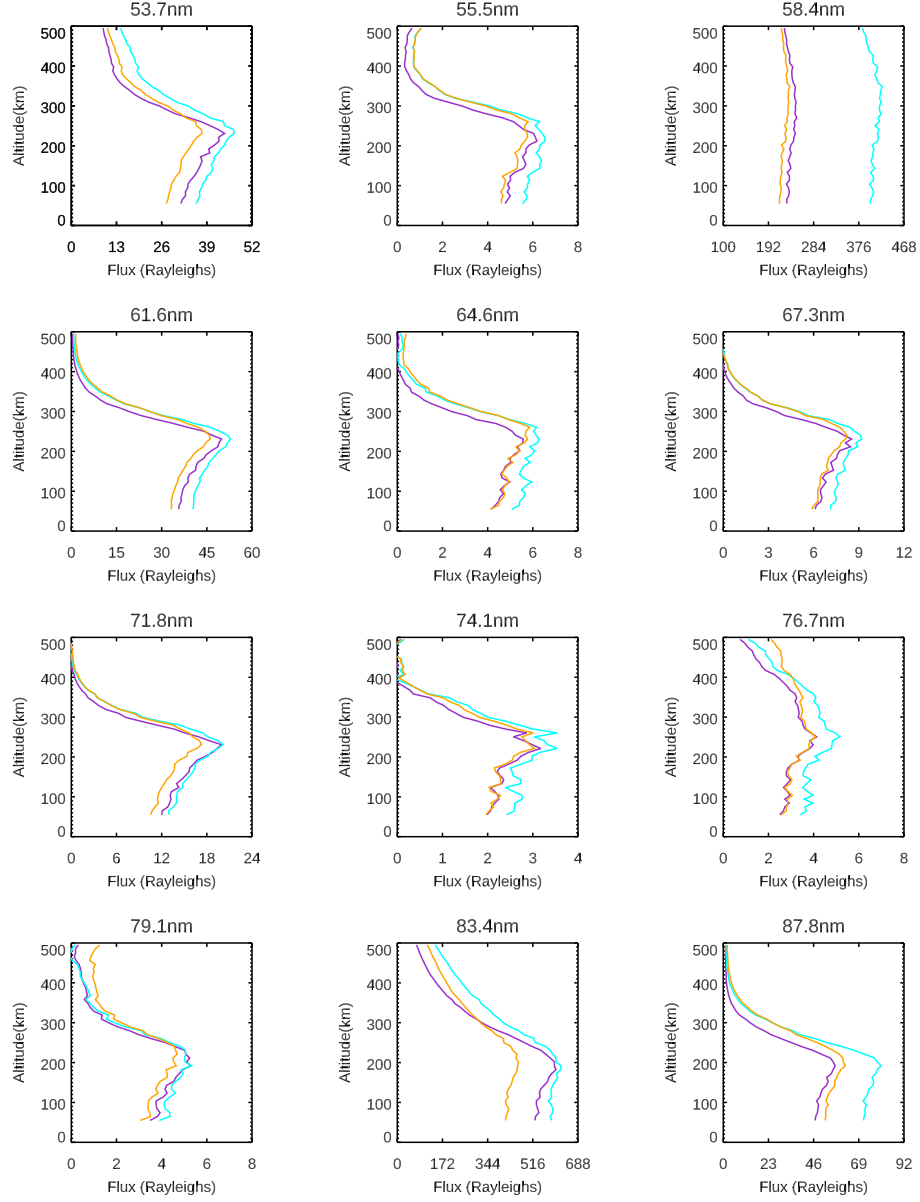
An EUV $\Sigma O/N_2$ retrieval algorithm offers a potential advantage over current FUV methods for retrieving $\Sigma O/N_2$. The 135.6 nm oxygen doublet used for FUV retrieval is dominated by photoionization excitation of O with minor, but often non-negligible, contributions from O^+ radiative recombination, especially at high altitudes. In certain regions and atmospheric conditions, this can lead to ionospheric contamination of the retrieved $\Sigma O/N_2$ (Kil et al., 2013). In contrast, the 61.6 nm line is only produced in significant amounts by photoionization excitation of O. This advantage could potentially offset the difficulty and uncertainties that arise from the dimness of the EUV features. An effective EUV retrieval of neutral composition would be practically advantageous since it would allow for the measurement of the neutral thermosphere and the ionosphere with a single instrument.
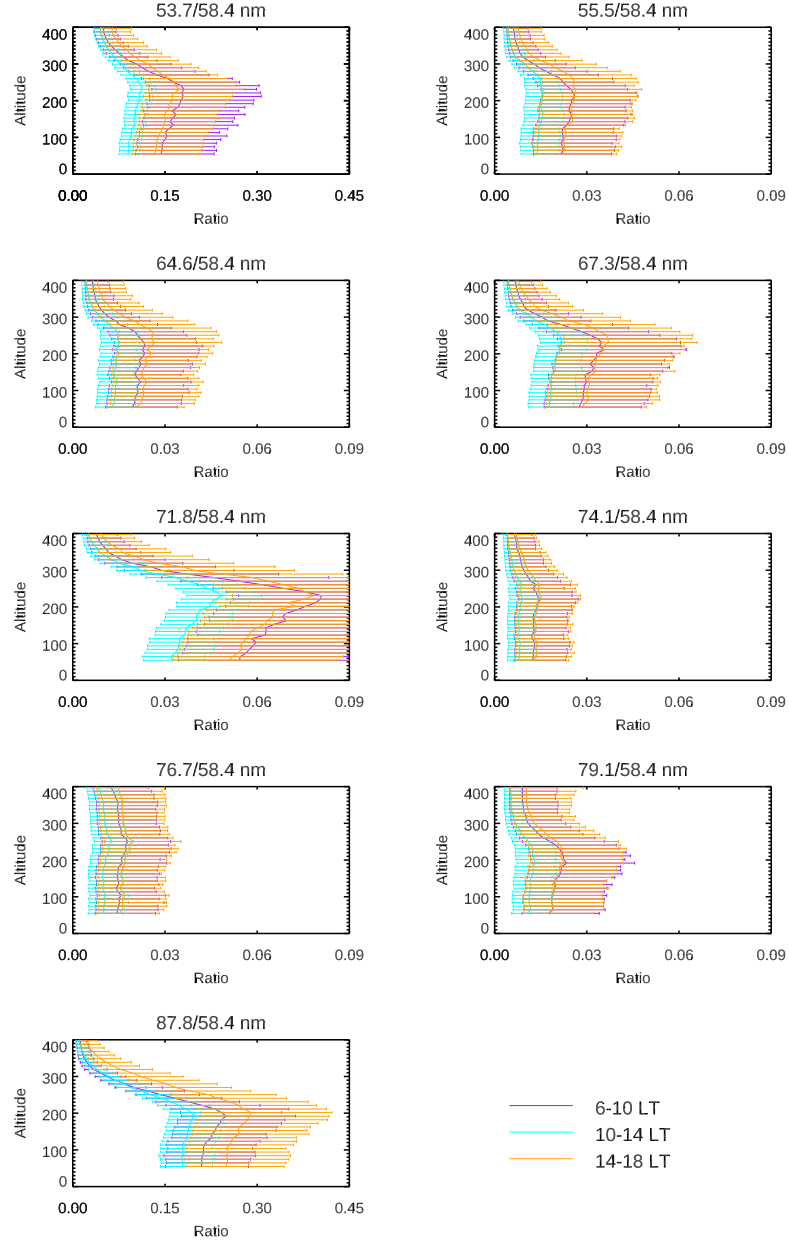
6 Data Availability Statement

This analysis used version 03 of the Level 1.5 ICON-EUV data, version 03 of the Level 1.3 ICON-FUV data, and version 03 of the ICON-Ancillary data which are available from the ICON website (`https://icon.ssl.berkeley.edu/Data`) and NASA's

492   Space Physics Data Facility (`https://cdaweb.gsfc.nasa.gov/pub/data/icon/`). The

493   NRLMSISE-00 model is available from NASA's Community Coordinated Modeling Cen-
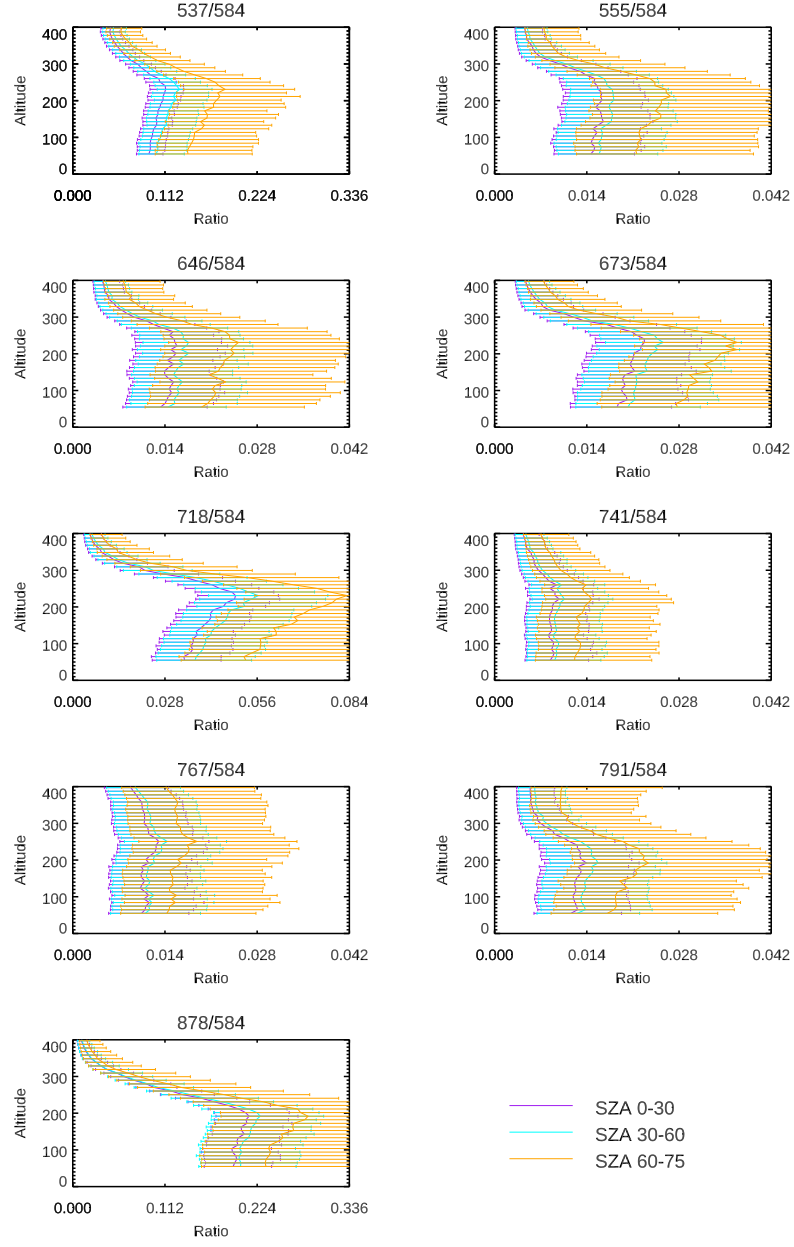
494   ter (`https://ccmc.gsfc.nasa.gov/pub/modelweb/`).

Appendix A Additional Figures

Figure A1. Averaged altitude profiles of ICON L1 EUV wavelength bin for 6-10 LT (purple), 10-14 LT (cyan), and 14-18 LT (orange) from 2020 DOY 1-328.
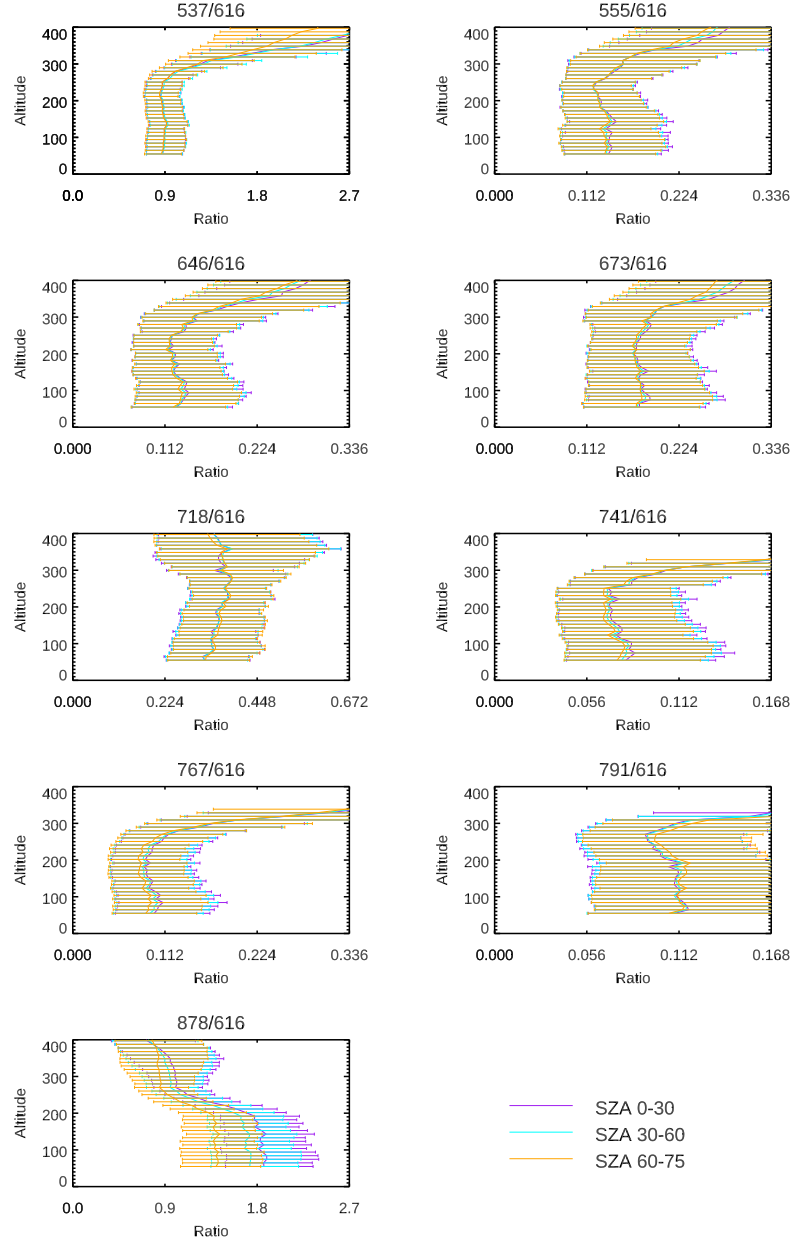
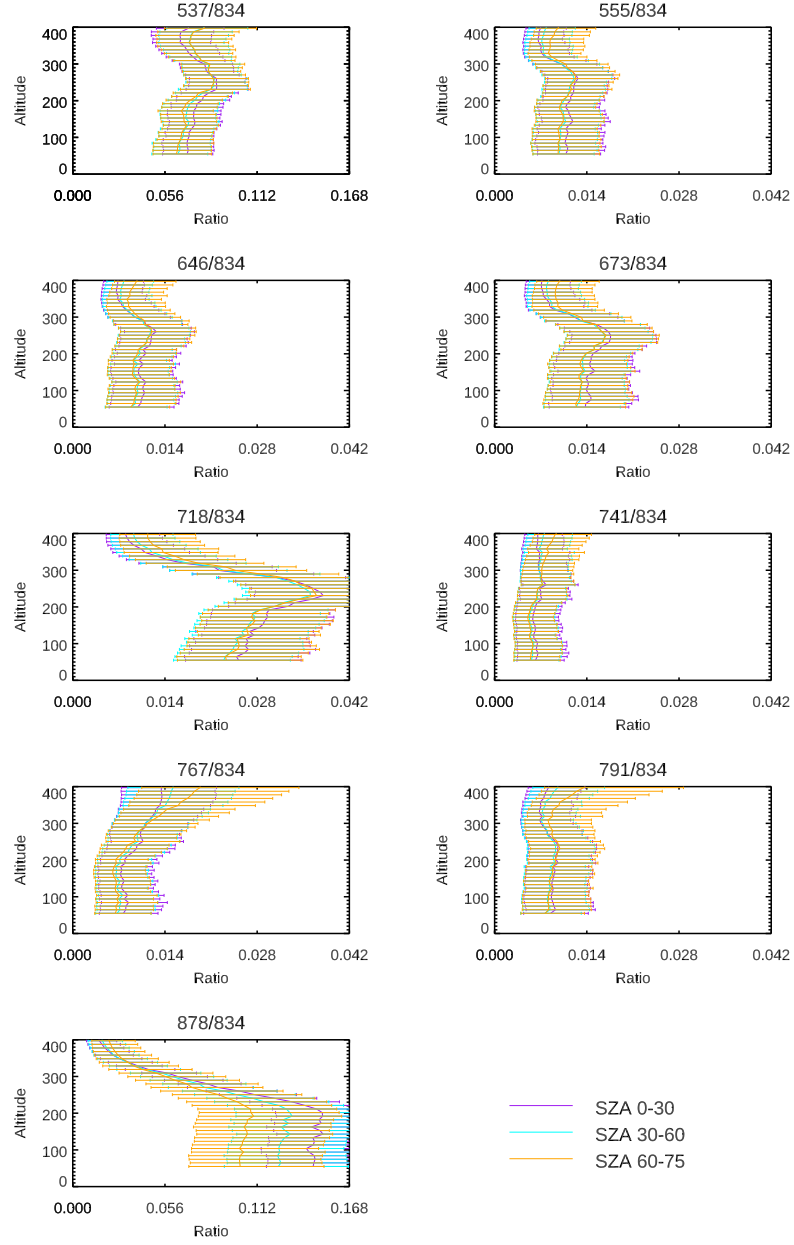**Figure A2.** Brightness relative to 58.4 nm brightness for each secondary line, broken down by LT.

Figure A3. Brightness relative to 58.4 nm brightness for each secondary line, broken down by SZA.

Figure A4. Brightness relative to 61.6 nm brightness for each secondary line, broken down by SZA.

Figure A5. Brightness relative to 83.4 nm brightness for each secondary line, broken down by SZA.

Acknowledgments

ICON is supported by NASA's Explorers Program through contracts NNG12FA45C and NNG12FA42I. RRM thanks the Civil Service Retirement System for partial support.

References

Anderson, J., D. E., Meier, R. R., & Weller, C. S. (1979, May). The seasonal-latitudinal variation of exospheric helium from He 584-A dayglow emissions. *Journal of Geophysical Research*, *84*(A5), 1914-1920. doi: 10.1029/ JA084iA05p01914

Boggs, P., & Donaldson, J. R. (1989). Orthogonal distance regression..

Bush, B. C., & Chakrabarti, S. (1995, October). Analysis of Lyman α and He I 584-Å airglow measurements using a spherical radiative transfer model. *Journal of Geophysical Research*, *100*(A10), 19609-19626. doi: 10.1029/95JA01210

Carlson, R. W., & Judge, D. L. (1973, May). Rocket observations of the extreme ultraviolet dayglow. *Planetary and Space Science*, *21*(5), 879-880. doi: 10.1016/ 0032-0633(73)90105-0

Carruthers, G. R., & Page, T. (1976, April). Apollo 16 Far ultraviolet spectra of the terrestrial airglow. *Journal of Geophysical Research*, *81*(10), 1683. doi: 10 .1029/JA081i010p01683

Chakrabarti, S., Paresce, F., Bowyer, S., Kimble, R., & Kumar, S. (1983, June). The extreme ultraviolet day airglow. *Journal of Geophysical Research*, *88*(A6), 4898-4904. doi: 10.1029/JA088iA06p04898

Christensen, A. B. (1976, April). A rocket measurement of the extreme ultraviolet dayglow. *Geophysical Research Letters*, *3*(4), 221-224. doi: 10.1029/GL003i004p00221

Conway, R. (1988, March). Photoabsorption and Photoionization Cross Sections of 0,02, and N2 for Photoelectron Production Calculations: A Compilation of Recent Laboratory Measurements, NRL Memorandum Report 6155 [Computer software manual].

Cotton, D. M., Chakrabarti, S., & Gladstone, G. R. (1993, December). Preliminary results from the Berkeley EUV airglow rocket spectrometer: O I and N_2 FUV/EUV dayglow in the thermosphere and lower exosphere. *Journal of Geophysical Research*, *98*(A12), 21627-21642. doi: 10.1029/93JA02267

Donahue, T. M., & Kumer, J. B. (1971, January). An observation of the helium I 584-A dayglow radiation between 400 and 1000 km. *Journal of Geophysical Research*, *76*(1), 145. doi: 10.1029/JA076i001p00145

Evans, J. S., Strickland, D. J., & Huffman, R. E. (1995, July). Satellite remote sensing of thermospheric O/N_2 and solar EUV. 2. Data analysis. *Journal of Geophysical Research*, *100*(A7), 12227-12234. doi: 10.1029/95JA00573

Fennelly, J. A., & Torr, D. G. (1992, January). Photoionization and Photoabsorption Cross Sections of O, N_2 O_2, and N for Aeronomic Calculations. *Atomic Data and Nuclear Data Tables*, *51*, 321. doi: 10.1016/0092-640X(92)90004-2

Gentieu, E. P., Feldman, P. D., & Meier, R. R. (1979, April). Spectroscopy of the extreme ultraviolet dayglow at 6.5Å resolution: Atomic and ionic emissions between 530 and 1240Å. *Geophysical Research Letters*, *6*(4), 325-328. doi: 10.1029/GL006i004p00325

Immel, T. J., England, S. L., Mende, S. B., Heelis, R. A., Englert, C. R., Edelstein, J., . . . Sirk, M. M. (2018, February). The Ionospheric Connection Explorer Mission: Mission Goals and Design. *Space Science Reviews*, *214*(1), 13. doi: 10.1007/s11214-017-0449-2

Kil, H., Lee, W. K., Shim, J., Paxton, L. J., & Zhang, Y. (2013). The effect of the 135.6 nm emission originated from the ionosphere on the timed/guvi o/n2 ratio. *Journal of Geophysical Research*, *118*(2), 859-865. Retrieved from `https://agupubs.onlinelibrary.wiley.com/doi/abs/10.1029/2012JA018112` doi: https://doi.org/10.1029/2012JA018112

Kramida, A., Yu. Ralchenko, Reader, J., & and NIST ASD Team. (2021). NIST Atomic Spectra Database (ver. 5.9), [Online]. Available: `https://physics.nist.gov/asd` [2022, March 30]. National Institute of Standards and Technology, Gaithersburg, MD.

Lean, J. L., Meier, R. R., Picone, J. M., & Emmert, J. T. (2011, October). Ionospheric total electron content: Global and hemispheric climatology. *Journal of Geophysical Research*, *116*(A10), A10318. doi: 10.1029/2011JA016567

Meier, R. R. (1991, December). Ultraviolet spectroscopy and remote sensing of the upper atmosphere. *Space Science Reviews*, *58*(1), 1-185. doi: 10.1007/BF01206000

Meier, R. R. (2021, March). The Thermospheric Column O/N_2 Ratio. *Journal of*

Geophysical Research, *126*(3), e29059. doi: 10.1029/2020JA029059

Meier, R. R., Picone, J. M., Drob, D., Bishop, J., Emmert, J. T., Lean, J. L., ...
Gibson, S. T. (2015). Remote sensing of earth's limb by timed/guvi: Retrieval
of thermospheric composition and temperature. *Earth and Space Science*, *2*(1),
1-37. Retrieved from `https://agupubs.onlinelibrary.wiley.com/doi/abs/`
`10.1002/2014EA000035` doi: https://doi.org/10.1002/2014EA000035

Meier, R. R., Samson, J. A. R., Chung, Y., Lee, E. M., & He, Z. X. (1991, August).
Production of N $^{+*}$ from N $_2$ + hv: Effective EUV emission yields from labo-
ratory and dayglow data. *Planetary and Space Science*, *39*(8), 1197-1207. doi:
10.1016/0032-0633(91)90171-6

Mende, S. B., Frey, H. U., Rider, K., Chou, C., Harris, S. E., Siegmund, O. H. W.,
... Ellis, S. (2017, October). The Far Ultra-Violet Imager on the Icon Mission.
Space Science Reviews, *212*(1-2), 655-696. doi: 10.1007/s11214-017-0386-0

Mendillo, M., Huang, C.-L., Pi, X., Rishbeth, H., & Meier, R. (2005, Octo-
ber). The global ionospheric asymmetry in total electron content. *Jour-
nal of Atmospheric and Solar-Terrestrial Physics*, *67*(15), 1377-1387. doi:
10.1016/j.jastp.2005.06.021

Picone, J. M., Hedin, A. E., Drob, D. P., & Aikin, A. C. (2002). Nrlmsise-00 em-
pirical model of the atmosphere: Statistical comparisons and scientific issues.
Journal of Geophysical Research, *107*(A12), SIA 15-1-SIA 15-16. Retrieved
from `https://agupubs.onlinelibrary.wiley.com/doi/abs/10.1029/`
`2002JA009430` doi: https://doi.org/10.1029/2002JA009430

Prölss, G. W., & Bird, M. K. (2004). *Physics of the Earth's Space Environment: an
introduction.*

Sirk, M. M., Korpela, E. J., Ishikawa, Y., Edelstein, J., Wishnow, E. H., Smith,
C., ... Immel, T. J. (2017, October). Design and Performance of the
ICON EUV Spectrograph. *Space Science Reviews*, *212*(1-2), 631-643. doi:
10.1007/s11214-017-0384-2

Stephan, A. W. (2016, September). Advances in remote sensing of the daytime iono-
sphere with EUV airglow. *Journal of Geophysical Research*, *121*(9), 9284-9292.
doi: 10.1002/2016JA022629

Stephan, A. W., Korpela, E. J., Sirk, M. M., England, S. L., & Immel, T. J. (2017,
October). Daytime Ionosphere Retrieval Algorithm for the Ionospheric Connec-

tion Explorer (ICON). *Space Science Reviews*, *212*(1-2), 645-654. doi: 10 .1007/s11214-017-0385-1

Stephan, A. W., Meier, R. R., England, S. L., Mende, S. B., Frey, H. U., & Immel, T. J. (2018, February). Daytime O/N$_2$ Retrieval Algorithm for the Ionospheric Connection Explorer (ICON). *Space Science Reviews*, *214*(1), 42. doi: 10.1007/s11214-018-0477-6

Stephan, A. W., Picone, J. M., Budzien, S. A., Bishop, R. L., Christensen, A. B., & Hecht, J. H. (2012, January). Measurement and application of the O II 61.7 nm dayglow. *Journal of Geophysical Research*, *117*(A1), A01316. doi: 10.1029/2011JA016897

Strickland, D. J., Evans, J. S., & Paxton, L. J. (1995, July). Satellite remote sensing of thermospheric O/N$_2$ and solar EUV. 1. Theory. *Journal of Geophysical Research*, *100*(A7), 12217-12226. doi: 10.1029/95JA00574

Strickland, D. J., Meier, R. R., Walterscheid, R. L., Craven, J. D., Christensen, A. B., Paxton, L. J., ... Crowley, G. (2004, January). Quiet-time seasonal behavior of the thermosphere seen in the far ultraviolet dayglow. *Journal of Geophysical Research*, *109*(A1), A01302. doi: 10.1029/2003JA010220

Young, J. M., Carruthers, G. R., Holmes, J. C., Johnson, C. Y., & Patterson, N. P. (1968, May). Detection of Lyman-β and Helium Resonance Radiation in the Night Sky. *Science*, *160*(3831), 990-991. doi: 10.1126/science.160.3831.990